

# RMMI: Enhanced Obstacle Avoidance for Reactive Mobile Manipulation using an Implicit Neural Map

Nicolás Marticorena, Tobias Fischer, Jesse Haviland, Niko Suenderhauf

**Abstract**—We introduce RMMI, a novel reactive control framework for mobile manipulators operating in complex, static environments. Our approach leverages a neural Signed Distance Field (SDF) to model intricate environment details and incorporates this representation as inequality constraints within a Quadratic Program (QP) to coordinate robot joint and base motion. A key contribution is the introduction of an active collision avoidance cost term that maximises the total robot distance to obstacles during the motion. We first evaluate our approach in a simulated reaching task, outperforming previous methods that rely on representing both the robot and the scene as a set of primitive geometries. Compared with the baseline, we improved the task success rate by 25% in total, which includes increases of 10% by using the active collision cost. We also demonstrate our approach on a real-world platform, showing its effectiveness in reaching target poses in cluttered and confined spaces using environment models built directly from sensor data. For additional details and experiment videos, visit <https://rmmi.github.io/>.

**Index Terms**—Mobile Manipulation, Collision Avoidance, Motion Control and Reactive Control

## I. INTRODUCTION

Recent advances in perception and control have significantly enhanced the capabilities of reactive controllers, allowing robots to adapt their actions dynamically based on real-time sensor data. These controllers enable robust task execution by continuously adjusting the robot’s behaviour, facilitating complex operations such as visual servoing and object manipulation during motion [1], [2].

Traditionally, reactive control has been valued for its speed and adaptability, though it was often considered less capable in handling complex environments compared to motion planning, which, while more capable, is typically slower and computationally intensive. Recent works in motion planning [3], [4] have made significant strides in improving computational efficiency, allowing for faster planning in dynamic and cluttered environments. These advancements are narrowing the gap between reactive control and motion planning, making them more comparable in terms of speed and capability.

Despite advances in reactive controllers for mobile manipulation, they still face challenges in collision avoidance. Existing methods often rely on simplified scene models, assuming perfect knowledge of the environment using geometric primitives [5]. Others extend 2D laser scan data vertically, which restricts the robot’s operation in confined spaces [6], [7]. Some approaches incorporate sensor data to build scene models, but the discrete nature of these representations leads

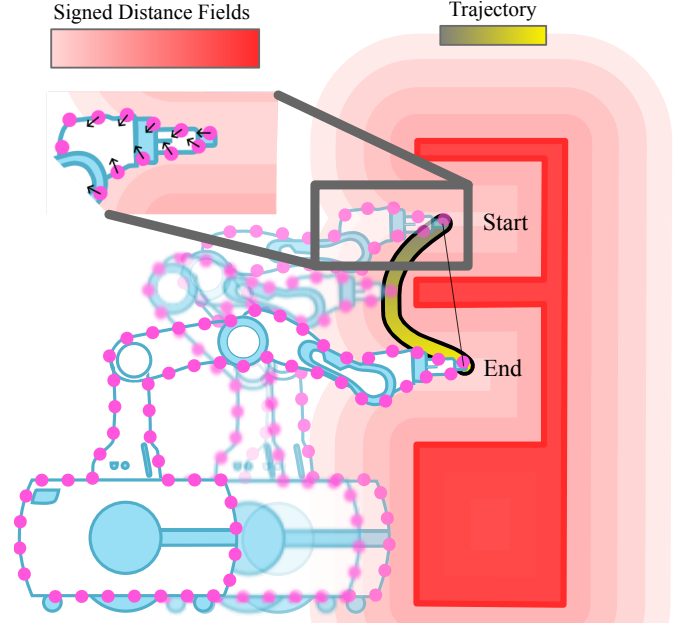


Fig. 1. Illustration of our approach to reactive control in cluttered environments. The obstacles are represented within a Signed Distance Field (SDF), shown in red, where darker shades indicate closer proximity to the obstacle surfaces. The robot is represented as a set of points sampled from its outer geometry (depicted as magenta dots). Our controller computes the joint velocities required to follow a trajectory from the start to the end pose (highlighted in yellow), while simultaneously maximising manipulability and maintaining a safe distance from obstacles, all within the constraints of joint limits and collision avoidance.

to approximations that limit the precision of collision detection [8]–[10].

To address these limitations, we propose a novel reactive controller that incorporates collision avoidance by querying a 3D representation of the robot’s surroundings, modelled as a neural Signed Distance Field (SDF). Unlike traditional methods, our approach leverages the continuous representation provided by the neural SDF, allowing for precise obstacle detection and efficient collision avoidance in cluttered environments. Another advantage of using neural SDFs are the fixed query times that lead to a consistent control rate.

Our method enhances collision avoidance by representing the robot’s outer geometry with sampled points. These points are queried against the SDF to determine their proximity to obstacles, and the resulting distance and direction data are incorporated into the controller’s optimisation as inequality constraints. Additionally, we introduce an active collision avoidance cost within the optimisation framework, which further increases the robot’s safety margin by maximising its distance from obstacles during motion. Notably, as shown

The authors are with the QUT Centre For Robotics, School of Electrical Engineering and Robotics at the Queensland University of Technology, Brisbane, QLD 4000, Australia. We acknowledge the ongoing support by the QUT Centre for Robotics. Email: nicolas.marticorena@hdr.qut.edu.au

in Fig. 1, our controller enables the robot to perform complex tasks, such as reaching target poses inside a bookshelf, with enhanced precision.

In summary, the contributions of this letter are:

- 1) The formulation of a reactive controller that incorporates collision avoidance in 3D, in which the robot is represented as a set of points sampled from its outer mesh. By obtaining the distance of each point using a neural Signed Distance Field, we formulate different inequality constraints that are incorporated into the controller optimisation problem.
- 2) The introduction of an active collision avoidance cost to the optimisation problem that steers the robot away from obstacles by averaging the individual distances projected in the robot’s configuration space. The active collision avoidance cost leads to a further average performance increase of 10% in task completion.
- 3) A thorough validation of our approach through simulated and real-world experiments, demonstrating its effectiveness in performing precise mobile manipulation tasks such as reaching target poses inside a bookshelf and behind objects on a cluttered table<sup>1</sup>. We also ablate the various components within our framework.

## II. RELATED WORKS

### A. Collision Avoidance in Motion Generation

Collision avoidance is a critical component in motion generation, with seminal work introducing artificial potential fields to formulate collision avoidance as virtual repulsive fields [11], [12]. Other approaches have incorporated collision avoidance within a Quadratic Programming (QP) framework, where it is treated as a set of hard inequality constraints [5], [7].

While effective, these methods often rely on simplified collision primitives or precise object models, limiting their applicability in unstructured environments [5], [11]. To address these limitations, some researchers have explored sensor-based approaches, using data from 2D laser scans on mobile manipulators [6], [7] or depth maps for static manipulators [12], [13]. However, these methods face challenges: 2D laser scans restrict the space in which a robot arm can operate, while depth maps are less practical for mobile manipulators due to limited viewing angles from robot-mounted cameras.

Our work advances these approaches by integrating a 3D representation that efficiently models collisions within a holistic reactive controller, eliminating the need for predefined geometric models and overcoming some of the limitations of purely sensor-based methods. The next section delves into the challenge of developing efficient representations for collision avoidance within the context of motion generation.

### B. Traditional Representations for Collision Avoidance

To *plan* collision-free motions, the robot requires a collision-checking routine; this routine needs to be *efficient* given the large number of configurations that are tested during

motion planning [14] and *fast* to avoid lowering the controller frequency [12]. This has led to significant research into developing representations that support efficient collision checking, particularly those derived directly from sensor information.

One widely used representation is the *occupancy-map*, where a 3D scene is represented as a grid of voxels, each indicating the probability of occupancy. A notable implementation is OctoMap [15], which segments the environment into “occupied” or “free” voxels, facilitating collision checking in sampling-based motion planning [16].

### C. Signed Distance Fields for Collision Checking

Another prevalent approach is the use of signed distance fields (SDF), which store the distance to the nearest surface. SDFs offer the advantage of direct distance information as well as gradient information [17], making them suitable for planning methods such as trajectory optimisation [18]. SDFs of a scene can be obtained by combining analytical distance functions [19], parameterisation inside a neural network [20], or stored in a voxel map [21], [22]. While voxel-based SDF maps have become popular in motion planning [18] and model predictive control [8]–[10], they suffer from discretisation issues, necessitating trilinear interpolation or local linear models to refine distance estimates [8].

In contrast, our approach uses a continuous SDF parameterised by a neural network [23]–[25], which eliminates the fixed resolution of voxels and provides more accurate distance queries. Leveraging modern neural network libraries like PyTorch, we can perform multiple queries in parallel on a GPU, allowing for more precise robot representations compared to voxel-based approaches. Other work focused on learning SDFs of individual objects in the context of robotics control [26].

Moreover, some researchers have explored modelling the robot itself as an SDF by learning the robot’s SDF using neural networks [27] or basis functions [28]. The robot’s SDF enables precise control by computing the distance between the robot and its environment using static RGB-D cameras [13] or external tracking systems [27], [28].

## III. BACKGROUND

This section provides an overview of the core components that underpin our approach: the holistic mobile manipulator motion controller (Section III-A) and the use of signed distance fields (SDFs) for precise environmental representation (Section III-B).

### A. Holistic Mobile Manipulator Motion Controller

Our approach builds on the task space reactive controller introduced by [1], which achieves desired end-effector poses by simultaneously using the degrees of freedom of the arm and the mobile base. This controller ensures that joint limits are respected and that the arm remains manoeuvrable throughout the trajectory.

At the core of this controller is a Quadratic Program (QP) that is designed to output the required joint velocities  $\dot{\mathbf{q}} \in \mathbb{R}^n$ ,

<sup>1</sup>Videos and 3D reconstructions are available on <https://rmmi.github.io/>

where  $n$  represents the degrees of freedom of the mobile manipulator, including both the arm and the base. The primary objective is to achieve the desired spatial velocity  $\mathbf{v} \in \mathbb{R}^6$  of the end-effector in the base frame  ${}^b\mathbf{v}_e^*$ , where  $e$  represents the end-effector frame and  $b$  the robot's base frame.

The optimisation problem is defined as the following QP formulation:

$$\min_{\mathbf{x}} \frac{1}{2} \mathbf{x}^\top \mathbf{Q} \mathbf{x} + \mathbf{c}^\top \mathbf{x} \quad (1)$$

$$\text{s.t. } \mathcal{J} \mathbf{x} = {}^b\mathbf{v}_e \quad (2)$$

$$\mathbf{A} \mathbf{x} \leq \mathbf{b} \quad (3)$$

$$\chi^- \leq \mathbf{x} \leq \chi^+ \quad (4)$$

Here the decision variable  $\mathbf{x}$  is a combination of the joint velocities  $\dot{\mathbf{q}}$  and a slack component  $\delta \in \mathbb{R}^6$ :

$$\mathbf{x} = \begin{pmatrix} \dot{\mathbf{q}} \\ \delta \end{pmatrix} \in \mathbb{R}^{(n+6)}. \quad (5)$$

The quadratic cost function defined in Eq. (1) is designed to minimise joint velocities, where the linear cost component  $\mathbf{c}$  is given by:

$$\mathbf{c} = \begin{pmatrix} \mathbf{J}_m + \mathbf{J}_o \\ \mathbf{0}_6 \end{pmatrix} \in \mathbb{R}^{(n+6)}, \quad (6)$$

with  $\mathbf{J}_m \in \mathbb{R}^n$  representing the manipulability Jacobian [29] that maximises the manipulability index of the robot arm [30], which indicates how well conditioned the current arm configuration is. The term  $\mathbf{J}_o \in \mathbb{R}^n$  comprises a linear component to optimise the base's relative orientation to the end-effector [1].

The equality constraints in Eq. (2) are implemented through an augmented manipulator Jacobian  $\mathcal{J}$  [29]:

$$\mathcal{J} = \begin{pmatrix} {}^b\mathbf{J}_e & \mathbf{1}_{6 \times 6} \end{pmatrix} \in \mathbb{R}^{6 \times (n+6)}, \quad (7)$$

where  ${}^b\mathbf{J}_e \in \mathbb{R}^{6 \times n}$  maps joint velocities to the end-effector's spatial velocity.

Inequality constraints in Eq. (3) enforce joint limits, and Eq. (4) defines bounds on the decision variable.

## B. Signed Distance Fields

Signed distance fields (SDF) are a well-studied representation of objects and environments that is widely used in robotics [17], computer vision [31], and computer graphics [32]. In the 3D case, an SDF is a function  $f: \mathbb{R}^3 \rightarrow \mathbb{R}$  that returns the distance  $d \in \mathbb{R}$  of a sample point  $\mathbf{p} \in \mathbb{R}^3$  to the nearest surface. The sign of this distance indicates if the sampled point  $\mathbf{p}$  is inside the surface (negative), outside (positive), or on the surface (zero distance). Consequently, the surface  $\mathcal{S}$  of the obstacle is represented by the zero-level set of the SDF:

$$\mathcal{S} = \{\mathbf{p} \in \mathbb{R}^3 | f(\mathbf{p}) = 0\}. \quad (8)$$

In addition, we can determine the direction to the closest obstacle by computing the gradient  $\hat{\mathbf{g}} \in \mathbb{R}^3$  of this function. This gradient vector points from the sampling point away from the surface, enabling the closest point on the surface  $\mathbf{p}_{\text{near}}$  to be estimated as [33]:

$$\mathbf{p}_{\text{near}} = \mathbf{p} - d \cdot \hat{\mathbf{g}}, \text{ where } d = f(\mathbf{p}), \text{ and } \hat{\mathbf{g}} = \nabla_{\mathbf{p}} f(\mathbf{p}). \quad (9)$$

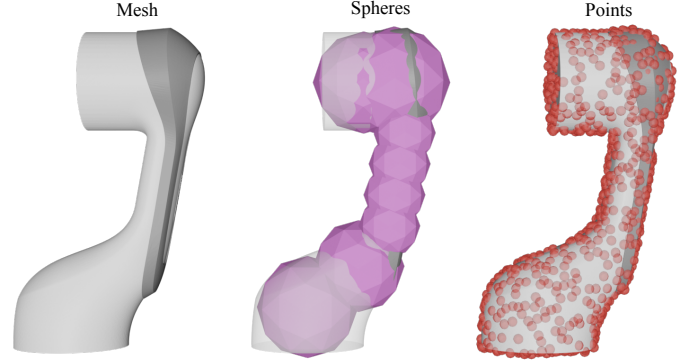


Fig. 2. Comparison of different representations for one of the robot's links. The left image shows the original mesh geometry. The centre image illustrates a manual sphere-based representation, where the geometry is approximated by overlapping spheres, which can result in inflated and imprecise regions [4]. The right image depicts our point-based representation, where points are sampled directly from the surface of the mesh, providing a more accurate and detailed representation of the robot's geometry.

In our approach, SDFs are integral to accurately representing the robot's environment, allowing for precise collision avoidance within our holistic motion controller.

## IV. METHODOLOGY

Our controller is formulated as a QP optimisation problem, building on the principles discussed in Section III-A. In this context, we integrate collision avoidance as both individual constraints and a secondary optimisation objective that maximises the robot's overall distance from obstacles. The methodology comprises three main steps: (1) representing the robot's geometry and querying the SDF based on sampled points from its outer mesh (Section IV-A), (2) formulating collision constraints to ensure safe navigation (Section IV-B), and (3) introducing an active collision avoidance cost within the optimisation to enhance safety margins (Section IV-C).

### A. Robot Representation

To effectively compute distances to obstacles using an SDF, the robot must be represented as a set of discrete points sampled from its outer mesh. These points, derived from the robot's URDF model, provide a detailed approximation of the robot's geometry.

In the first step, we group the various meshes corresponding to the robot's links according to the final joint in their respective kinematic chains. For each of these grouped meshes, we sample a set of points  ${}^k\mathbf{p}_j \in \mathbb{R}^3$  for the  $j$ -th point on the  $k$ -th link. The complete set of sampled points,  ${}^k\mathcal{P}$  for the  $k$ -th link is represented as:

$${}^k\mathcal{P} = \{{}^k\mathbf{p}_j | j = 1, \dots, M_k\}, \quad (10)$$

where  $M_k$  is the total number of points sampled from the  $k$ -th link.

These points are then transformed into the world reference frame using the rigid body transformation  ${}^w\mathbf{T}_k \in SE(3)$  obtained through forward kinematics:

$${}^w\mathcal{P} = \bigcup_k \{{}^w\mathbf{T}_k \cdot {}^k\mathbf{p}_j | {}^k\mathbf{p}_j \in {}^k\mathcal{P}\}. \quad (11)$$

This operation results in a set of  $N$  points, where  $N = \sum_k M_k$  represents the total number of points sampled from the entire robot. An illustration comparing this points-based representation to a traditional sphere-based approach [4] is shown in Fig. 2, highlighting the precision of our method in capturing the robot's geometry.

### B. Collision Constraints

With the robot represented as a set of sampled points and capable of querying the SDF for distance information, the next step is to incorporate these distances into the QP as hard constraints. Following [5], we account for how joint movements affect the distances between the robot and obstacles. At every step  $t$ , the distance of the  $j$ -th sampled point to an obstacle is defined as:

$$d_j(t) = f({}^w\mathbf{p}_j(t)). \quad (12)$$

Moving forward, the subscript  $j$  is omitted for ease of notation and compactness.

By taking the derivative of this distance with respect to time by applying the chain rule, we obtain

$$\dot{d}(t) = \nabla_{\mathbf{p}} f(\mathbf{p}) \cdot {}^w\dot{\mathbf{p}}(t) = \hat{\mathbf{g}} \cdot {}^w\dot{\mathbf{p}}(t). \quad (13)$$

Here,  ${}^w\dot{\mathbf{p}}(t)$  represents the translational velocity of the point, which can be expressed using the manipulator Jacobian  $\mathbf{J}_{\nu}(\tilde{\mathbf{q}}) \in \mathbb{R}^{(3 \times k)}$  considering each point as the end-effector [29], where  $\tilde{\mathbf{q}} = (q_0, q_1, \dots, q_k) \in \mathbb{R}^k$  denotes the joints up to the  $k$ -th link. Rewriting  ${}^w\dot{\mathbf{p}}(t)$  with respect to the joint's velocity results in:

$${}^w\dot{\mathbf{p}}(t) = \mathbf{J}_{\nu}(\tilde{\mathbf{q}})\dot{\tilde{\mathbf{q}}}(t). \quad (14)$$

Substituting this into the derivative of the distance, we obtain:

$$\hat{\mathbf{g}} \cdot \mathbf{J}_{\nu}(\tilde{\mathbf{q}}) \cdot \tilde{\mathbf{q}} = \dot{d}(t), \quad (15)$$

which relates the change in distance to the joint velocities. Following [5], we define the distance Jacobian  $\mathbf{J}_{d_j}$  for each point:

$$\mathbf{J}_{d_j}(\tilde{\mathbf{q}}_j) = \hat{\mathbf{g}}_j \cdot \mathbf{J}_{\nu_j}(\tilde{\mathbf{q}}_j). \quad (16)$$

Using a general velocity damper [34], we impose the following inequality:

$$\mathbf{J}_{d_j}(\tilde{\mathbf{q}})\dot{\tilde{\mathbf{q}}}(t) \leq \frac{f({}^w\mathbf{p}_j) - d_s}{d_i - d_s}, \quad (17)$$

where  $d_i$  is the influence distance, i.e. the distance where the point is considered in the optimisation, and  $d_s$  is the stopping distance, i.e. the minimum allowable distance to an obstacle.

Stacking these inequalities for all points results in the following matrix-vector relation:

$$\begin{pmatrix} \mathbf{J}_{d_1}(\tilde{\mathbf{q}}_1)\tilde{\mathbf{q}}_1 & \mathbf{0}_{1 \times 6+n-k_1} \\ \vdots & \vdots \\ \mathbf{J}_{d_N}(\tilde{\mathbf{q}}_N)\tilde{\mathbf{q}}_N & \mathbf{0}_{1 \times 6+n-k_N} \end{pmatrix} \mathbf{x}(t) \leq \begin{pmatrix} \frac{f(\mathbf{p}_1) - d_s}{d_i - d_s} \\ \vdots \\ \frac{f(\mathbf{p}_N) - d_s}{d_i - d_s} \end{pmatrix} \quad (18)$$

where the matrix on the left side is defined as  $\mathbf{A}_c \in \mathbb{R}^{N \times n+6}$ , and the right side vector as  $\mathbf{b}_c \in \mathbb{R}^N$ . Both can be integrated into the QP via Eq. (3).

### C. Active Collision Avoidance

Beyond the hard constraints, we introduce a collision avoidance cost into the objective function, promoting trajectories that maximise the robot's distance from obstacles.

To formulate this cost, we define a collision Jacobian  $\mathbf{J}_c$  to represent how the distance between the robot and obstacles changes with respect to the joint velocities. This Jacobian is calculated as a weighted average of the individual distance Jacobians  $\mathbf{J}_{d_j}$ , with weights proportional to the distances:

$$\mathbf{J}_c = \frac{\sum \mathbf{J}_{d_j}(\mathbf{q}_j)w(\mathbf{p}_j)}{\sum w(\mathbf{p}_j)}, \quad (19)$$

where the weight function  $w(\mathbf{p}_j)$  is defined as:

$$w(\mathbf{p}_j) = \frac{d_i - f(\mathbf{p}_j)}{d_i - d_s}. \quad (20)$$

However,  $\mathbf{J}_c$  is a normalised direction; to consider a cost that is dependent on the robot distance, we introduce a dynamic gain  $\lambda_c$ , inspired by the collision cost in CHOMP [18]:

$$\lambda_c(t) = \frac{\lambda_c^{max}}{(d_i - d_s)^2} \cdot (r_d(t) - d_i)^2, \quad (21)$$

where  $r_d$  is the distance of the robot as  $\min_j f({}^w\mathbf{p}_j)$ , and  $\lambda_c^{max}$  controls the steepness of the active collision gain.

Finally, we incorporate this collision cost into the overall optimisation:

$$\mathbf{c} = \begin{pmatrix} \mathbf{J}_m + \mathbf{J}_o + \lambda_c \mathbf{J}_c \\ \mathbf{0}_6 \end{pmatrix} \in \mathbb{R}^{(n+6)}. \quad (22)$$

This overall optimisation encourages the robot to maintain a safer distance from obstacles while optimising for manipulability and orientation.

## V. EVALUATION IN SIMULATION

To rigorously evaluate the effectiveness of our proposed method, we conducted extensive experiments in both simulated (this section) and real-world environments (Section VI). The simulation experiments provide a controlled setting to test the performance under varying conditions, while the real-world experiments validate the practicality and robustness of our approach in real-time applications.

### A. Setup

1) *Robot Platform*: For both the simulated and real-world experiments, we used Frankie<sup>2</sup>, a custom mobile manipulator platform consisting of a 7-degrees of freedom (DoF) Franka Panda arm mounted on a non-holonomic differential robot base, the Omron LD-60.

2) *Tasks*: The first set of experiments involved a reaching task, simulated using the Swift simulator and the Robotics Toolbox for Python [35]. The SDFs representing the obstacles were generated by combining analytic distance functions of primitive geometries [19].

We designed two environments, denoted as Bookshelf and Table, as illustrated in Fig. 3. In the Bookshelf environment

<sup>2</sup>[https://github.com/qcr/frankie\\_docs](https://github.com/qcr/frankie_docs)

TABLE I

RESULTS OF THE SIMULATED REACHING TASK, RESULTS ARE AVERAGED ACROSS 1000 VARIATIONS. OUR APPROACH ACHIEVES COLLISION-FREE MOTIONS, WHEREAS PREVIOUS METHODS RESULT IN COLLISIONS DUE TO THE PRIMITIVES NOT FULLY COVERING THE ROBOT’S GEOMETRY. ADDITIONALLY, THE COMBINATION OF BOTH COLLISION AVOIDANCE COMPONENTS IN OUR METHOD YIELDS THE HIGHEST SUCCESS RATES.

Method	Collision model	Robot representation	Active Collision Avoidance Cost IV-C	Success Rate (%) $\uparrow$	Collisions $\downarrow$	$\langle  \mathbf{a}  \rangle (m/s^2) \downarrow$
Holistic [1]	-	-	$\times$	18.8	81.2	0.671
Baseline [5] + [1]	Mesh-to-mesh	34 Primitives [35]	$\times$	50.2	45.6	0.740
Baseline w active cost	Mesh-to-mesh	34 Primitives [35]	$\checkmark$	59.1	35.3	0.733
Ours w/o active cost	SDF	82 Spheres [4]	$\times$	78.4	0	0.777
Ours	SDF	82 Spheres [4]	$\checkmark$	85.8	0	0.558
Ours w/o active cost	SDF	2358 points	$\times$	66.3	0	0.742
Ours	SDF	2358 points	$\checkmark$	79.5	0	<b>0.462</b>
Ours w/o active cost	SDF	9476 points	$\times$	75.5	0	0.699
Ours	SDF	9476 points	$\checkmark$	<b>88.5</b>	0	0.491

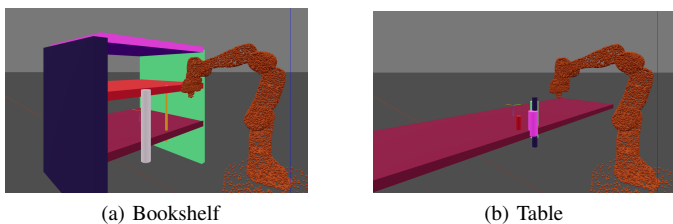


Fig. 3. Simulated environments in the Swift simulator: (a) Bookshelf and (b) Table. Each scene was varied across 500 iterations by randomly sampling the position and size of the obstacles, providing a diverse set of scenarios for evaluating the robot’s performance in reaching tasks.

(Fig. 3a), the heights of the top and bottom shelves, as well as the position and size of two cylinders placed on the front side of the bookshelf, were randomly varied. Similarly, in the Table environment (Fig. 3b), the height of the table and the position and size of four cylinders were randomly sampled.

We generated 500 different variations for each scenario, ensuring that any combination where the target pose resulted in a collision between the end-effector and obstacles was excluded.

3) *Metrics*: The following metrics were used to evaluate and compare the different approaches:

- **Success**: The success rate of the controller in generating a collision-free trajectory that reaches the desired 6-DoF pose with a margin of 2 cm as previous work [36].
- **Collisions**: The rate of robot collisions with the environment, used to distinguish task failures caused by local minima from those caused by collisions.
- **Gracefulness**: A proxy for the smoothness of motion, defined as being safe, comfortable, fast, and intuitive [37]. Following previous work [2], we measure the average absolute end-effector accelerations across different trials and environments, considering only successful motions to exclude cases where the robot failed due to local minima.

4) *Baselines*: We compare our approach against the holistic mobile manipulation controller presented in [1] and a modified version incorporating the collision avoidance component of NEO [5]. This provided a baseline for comparing the use of an implicit SDF versus mesh-to-mesh collision queries using primitives. Additionally, we tested our controller with two sets

of sampled points and a modified version<sup>3</sup> of the manually placed spheres from [4] to represent the robot. Finally, because our active collision avoidance is built by combining multiple inequality constraints, we included an experiment using the baseline [1] that incorporates our active collision cost.

## B. Results

The results of the simulation experiments are presented in Table I. Our approach, which integrates collisions constraints and a secondary cost function, achieved the highest performance, avoiding collisions in all attempts. When comparing our approach using variations on the robot representation by using different sets of sampled points alongside a robot representation using manually placed spheres. The approach reached a success rate of 88.5% for a point representation with 9476 points (with 11.5% getting stuck in local minima), followed by the manually placed spheres with 85.8%. When reducing the number of sampled points, the performance gradually reduces, with a 79.5% success rate when using 2358 points (see also Fig. 4).

In contrast, running the controller without any collision awareness failed in 81% of the runs. Modelling both the robot and the scene as geometric primitives yielded a success rate near 60%, with a collision rate of at least 35% due to the primitives not fully capturing the robot’s geometry.

## C. Ablations Studies

To further investigate the robustness of our method, we conducted ablation studies focusing on the precision of point sampling and the combination of the different collision avoidance components in the optimisation.

1) *Precision*: We evaluated our approach using different levels of precision in the robot representation, achieved by varying the total number of sampled points. As shown in Fig. 4, reducing the number of sampled points increased the controller frequency at the cost of performance. The reduced precision required a higher stopping distance to prevent interpenetration, resulting in less information being available to the control problem. For our real robot experiments, we selected the 2358 point representation, which offered the fastest controller frequency without reducing the success rate below 75%.

<sup>3</sup>The modification considers adding the Omron LD-60 Base.

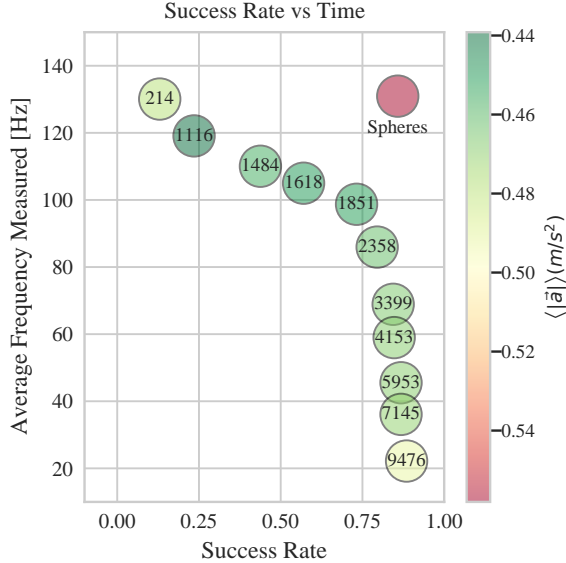


Fig. 4. Comparison of point representations using different levels of precision, where a faster control loop frequency is achieved at the cost of reduced performance in our benchmark tasks. The figure shows that as the number of sampled points decreases, the success rate drops, but the control loop operates at a higher frequency. Additionally, our approach using points instead of spheres results in smoother motions, as indicated by the lower average end-effector acceleration.

2) *Effects of Active Collision*: We tested various combinations of our collision avoidance components, including a sweep on  $\lambda_c^{max}$  to control the gain of the active collision cost. These combinations were tested on an additional 100 variations of both simulated environments to avoid overlap between data used for hyperparameter tuning and method evaluation. The results are shown in Fig. 5, where the dashed lines represent the baseline without the active collision cost, the dotted lines show the performance with only active collision cost, and the solid lines depict our full proposed approach. The results indicate that using both the inequality constraints and the active collision cost improved the success rate across different sampled point variations and the sphere representation. However,  $\lambda_c^{max} \geq 1.5$  led to diminishing returns, as the robot began prioritising obstacle avoidance over moving towards the goal.

## VI. REAL ROBOT EXPERIMENTS

Following the promising results in simulation, we conducted experiments on a real robot to validate the practical effectiveness of our approach in complex, real-world environments.

### A. Robot Representation

The robot representation used in the real-world experiments differs slightly from the simulation due to additional hardware considerations. Specifically, the real robot includes a RealSense D435 camera mounted on the end effector for capturing posed depth images, as well as a safety laser on the robot base. These additions required the inclusion of extra points and spheres to account for the camera and to extend the base representation, ensuring that the safety region where the mobile base operates is adequately covered.

( $\rightarrow$ ) 9476 Points ( $\rightarrow$ ) 2358 Points ( $\rightarrow$ ) Spheres

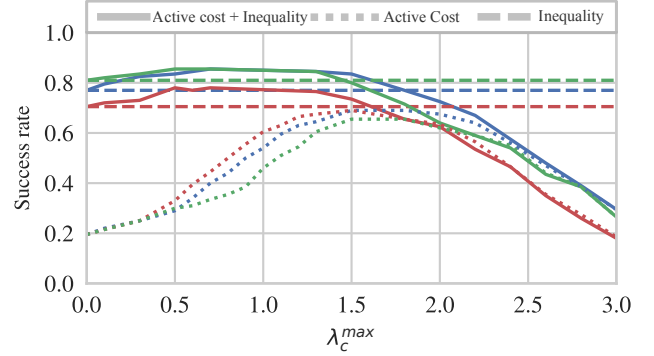


Fig. 5. Impact of varying the maximum gain  $\lambda_c^{max}$  on the success rate, averaged across both simulated scenes. The results demonstrate that combining both inequality constraints and the active collision cost yields the highest performance across different robot representations.

### B. Tasks and Setup

We evaluated our method in three real-world scenarios, as shown in Figure 6, with further details available in the supplementary video and on our website<sup>4</sup>. Each scene was reconstructed using iSDF [23] to generate the neural SDF from 30 pairs of posed depth images captured by the robot.

The experiments involved a reaching task with pre-defined target end-effector poses in three scenes. For the Cabinet and Bookshelf scenes, we tested four target poses, while the Table scene involved eight target poses. Each target pose was tested five times, resulting in a total of 80 trials per experiment. In each trial, the robot started with the arm in a home configuration, and the base was positioned randomly in front of the scene.

We compared our approach using both the manually placed spheres and our point-based representation, with and without our active collision avoidance cost. These methods were compared against a baseline controller without any collision awareness [1].

### C. Results

Some examples of the starting configurations and target poses are shown in Fig. 6 and the attached video. The results across the three different scenes are presented in Table II. Our approach, which incorporates both the inequality constraints and active collision cost, achieved the highest performance, with 96.3% and 97.5% for the point-based and sphere-based representations, respectively. Importantly, our method did not result in any collisions, with failures occurring only due to local minima.

The addition of the active collision cost significantly improved performance by at least 12.5% for both point-based and sphere-based robot representations. Without collision avoidance, the robot collided in 45% of the runs, with an additional 25% of failures due to the robot becoming stuck when obstacles intruded the safety zone of the base.

Interestingly, the end-effector acceleration measurements revealed a 10% reduction in acceleration when using the sphere-based representation compared to the point-based one. This

<sup>4</sup><https://rmmi.github.io>

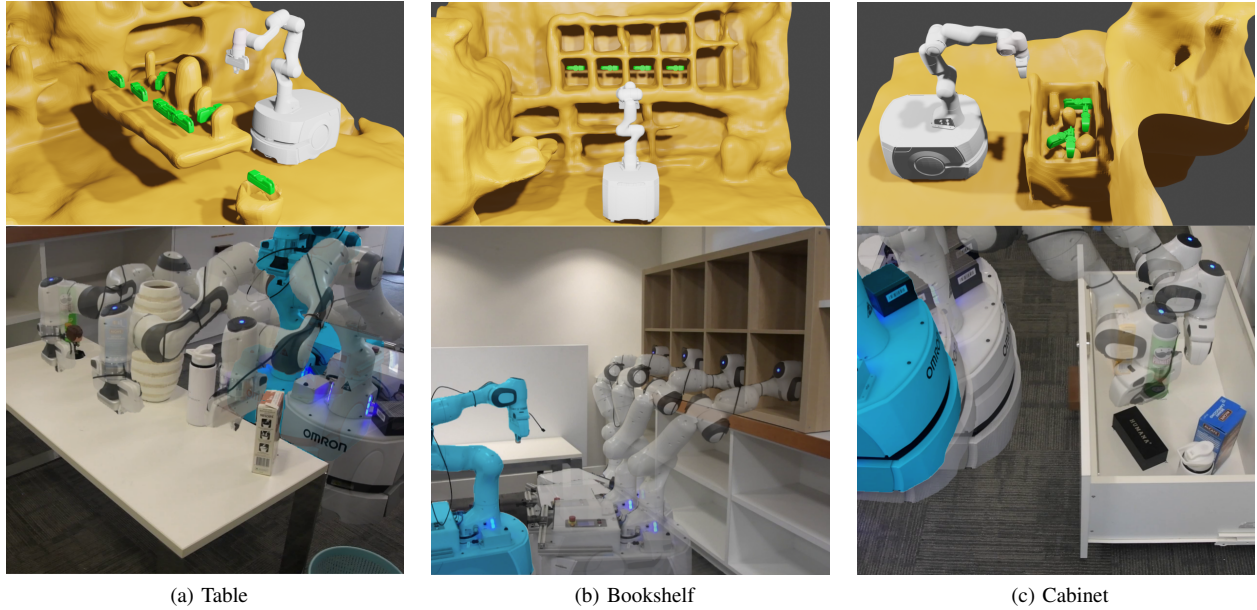


Fig. 6. (Top) Reconstructed meshes of the environments used for the real-world experiments: (a) Table, (b) Bookshelf, and (c) Cabinet. The green markers indicate the target 6-DoF poses for the robot's end effector in each scenario. (Bottom) Examples of the starting (blue) and final configurations of the robot during the experiments.

TABLE II  
REAL-WORLD EXPERIMENT RESULTS. OUR APPROACH SUCCESSFULLY ACHIEVED COLLISION-FREE MOTIONS ACROSS ALL SCENARIOS. BY COMBINING BOTH THE INEQUALITY CONSTRAINTS AND THE ACTIVE COLLISION COST, WE OBTAINED THE HIGHEST SUCCESS RATE.

		Collision cost	Success	Collisions	$\langle  a  \rangle (m/s^2)$
Bookshelf	[1]	×	0/20	0/20	0.19
	Points	×	13/20	0/20	0.29
		✓	20/20	0/20	0.39
	Spheres	×	19/20	0/20	0.33
		✓	19/20	0/20	0.36
	Cabinet	[1]	×	10/20	10/20
Points		×	20/20	0/20	0.35
		✓	19/20	0/20	0.31
Spheres		×	19/20	0/20	0.36
		✓	19/20	0/20	0.24
Table		[1]	×	14/40	26/40
	Points	×	28/40	0/20	0.28
		✓	38/40	0/20	0.29
	Spheres	×	30/40	0/20	0.31
		✓	40/40	0/20	0.30
	Total	[1]	×	24/80	36/80
Points		×	61/80	0/80	0.31
		✓	77/80	0/80	0.33
Spheres		×	68/80	0/80	0.34
		✓	78/80	0/80	0.30

contrasts with the simulation results, where the opposite was the case. We expect that this is due to the higher refresh rate of the real-world controller with the sphere representation. In the simulations, the control loop was executed at a fixed rate

across all representations.

## VII. CONCLUSIONS

In this letter, we presented a reactive controller capable of reliably reaching target poses while avoiding static obstacles, achieving a success rate of 96% in real-world tasks. Leveraging a neural SDF, our approach efficiently integrates collision avoidance into the reactive controller, while maintaining a fixed control rate. In addition, we introduced a simple yet effective active collision cost, which is robust to parameter variations and increases the performance by at least 10% in both simulation and real-world experiments.

Our approach effectively generates collision-free motions in a holistic manner, demonstrating robustness and efficiency. Limitations of our approach include the shortsightedness inherent in the local reactive controller paradigm, which makes our approach susceptible to local minima. This limitation could be mitigated by complementing our controller with a global planning strategy that updates at a lower frequency. Moreover, the parallel computation of distances enables our controller to operate a receding horizon framework.

Our approach opens promising avenues for future research. One potential direction is to eliminate the assumption of a predefined camera path for reconstruction [23], [24]. Integrating our controller with advances in the the Neural Fields community [38] could allow for the autonomous generation of these representations using a robot, paving the way for more dynamic and adaptive control strategies.

In conclusion, our reactive controller offers a robust and efficient solution for avoiding collisions with static obstacles, while also providing a foundation for future research that could further enhance its capabilities and applicability in complex robotic tasks.

## REFERENCES

- [1] J. Haviland, N. Sunderhauf, and P. Corke, "A Holistic Approach to Reactive Mobile Manipulation," *IEEE Robotics and Automation Letters*, vol. 7, no. 2, pp. 3122–3129, 2022.
- [2] B. Burgess-Limerick, C. Lehnert, J. Leitner, and P. Corke, "An Architecture for Reactive Mobile Manipulation On-The-Move," in *IEEE International Conference on Robotics and Automation*, 2023, pp. 1623–1629.
- [3] W. Thomason, Z. Kingston, and L. E. Kavraki, "Motions in microseconds via vectorized sampling-based planning," in *IEEE International Conference on Robotics and Automation*, 2024, pp. 8749–8756.
- [4] B. Sundaralingam, S. Kumar, S. Hari, A. Fishman, C. Garrett, K. V. Wyk, V. Blukis, A. Millane, H. Oleynikova, A. Handa, F. Ramos, N. Ratliff, and D. Fox, "CuRobo : Parallelized Collision-Free Robot Motion Generation," *IEEE International Conference on Robotics and Automation*, pp. 8112–8119, 2023.
- [5] J. Haviland and P. Corke, "NEO: A novel expeditious optimisation algorithm for reactive motion control of manipulators," *IEEE Robotics and Automation Letters*, vol. 6, no. 2, pp. 1043–1050, 2021.
- [6] B. Burgess-Limerick, J. Haviland, C. Lehnert, and P. Corke, "Reactive Base Control for On-the-Move Mobile Manipulation in Dynamic Environments," *IEEE Robotics and Automation Letters*, vol. 9, no. 3, pp. 2048–2055, 2024.
- [7] A. Heins, M. Jakob, and A. P. Schoellig, "Mobile Manipulation in Unknown Environments with Differential Inverse Kinematics Control," *Conference on Robots and Vision*, pp. 64–71, 2021.
- [8] J. Pankert and M. Hutter, "Perceptive model predictive control for continuous mobile manipulation," *IEEE Robotics and Automation Letters*, vol. 5, no. 4, pp. 6177–6184, 2020.
- [9] J. R. Chiu, J. P. Sleiman, M. Mittal, F. Farshidian, and M. Hutter, "A Collision-Free MPC for Whole-Body Dynamic Locomotion and Manipulation," *IEEE International Conference on Robotics and Automation*, pp. 4686–4693, 2022.
- [10] M. Mittal, D. Hoeller, F. Farshidian, M. Hutter, and A. Garg, "Articulated Object Interaction in Unknown Scenes with Whole-Body Mobile Manipulation," *IEEE/RSJ International Conference on Intelligent Robots and Systems*, pp. 1647–1654, 2022.
- [11] O. Khatib, "Real-time obstacle avoidance for manipulators and mobile robots," *IEEE International Conference on Robotics and Automation*, pp. 500–505, 1985.
- [12] A. Tulbure and O. Khatib, "Closing the loop: Real-time perception and control for robust collision avoidance with occluded obstacles," *IEEE/RSJ International Conference on Intelligent Robots and Systems*, pp. 5700–5707, 2020.
- [13] V. Vasilopoulos, S. Garg, P. Piacenza, J. Huh, and V. Isler, "Ramp: Hierarchical reactive motion planning for manipulation tasks using implicit signed distance functions," in *IEEE/RSJ International Conference on Intelligent Robots and Systems*, 2023, pp. 10 551–10 558.
- [14] J. Pan and D. Manocha, "GPU-based parallel collision detection for fast motion planning," *The International Journal of Robotics Research*, vol. 31, no. 2, pp. 187–200, 2012.
- [15] A. Hornung, K. M. Wurm, M. Bennewitz, C. Stachniss, and W. Burgard, "OctoMap: An efficient probabilistic 3D mapping framework based on octrees," *Autonomous Robots*, vol. 34, no. 3, pp. 189–206, 2013.
- [16] B. Arbanas, A. Ivanovic, M. Car, M. Orsag, T. Petrovic, and S. Bogdan, "Decentralized planning and control for UAV–UGV cooperative teams," *Autonomous Robots*, vol. 42, no. 8, pp. 1601–1618, 2018.
- [17] H. Oleynikova, A. Millane, Z. Taylor, E. Galceran, J. Nieto, and R. Siegwart, "Signed Distance Fields: A Natural Representation for Both Mapping and Planning," in *RSS Workshop: Geometry and Beyond - Representations, Physics, and Scene Understanding for Robotics*, 2016.
- [18] M. Zucker, N. Ratliff, A. D. Dragan, M. Pivtoraiko, M. Klingensmith, C. M. Dellin, J. A. Bagnell, and S. S. Srinivasa, "CHOMP: Covariant Hamiltonian optimization for motion planning," *International Journal of Robotics Research*, vol. 32, no. 9-10, pp. 1164–1193, 2013.
- [19] I. Quilez. 3d sdf primitives. [Online]. Available: <https://iquilezles.org/articles/distfunctions/>
- [20] J. J. Park, P. Florence, J. Straub, R. Newcombe, and S. Lovegrove, "DeepSDF: Learning continuous signed distance functions for shape representation," *IEEE Conference on Computer Vision and Pattern Recognition*, pp. 165–174, 2019.
- [21] H. Oleynikova, Z. Taylor, M. Fehr, R. Siegwart, and J. Nieto, "Voxblox: Incremental 3D Euclidean Signed Distance Fields for on-board MAV planning," *IEEE/RSJ International Conference on Intelligent Robots and Systems*, pp. 1366–1373, 2017.
- [22] Y. Pan, Y. Kompis, L. Bartolomei, R. Mascaro, C. Stachniss, and M. Chli, "Voxfield: Non-Projective Signed Distance Fields for Online Planning and 3D Reconstruction," in *IEEE/RSJ International Conference on Intelligent Robots and Systems*, 2022, pp. 5331–5338.
- [23] J. Ortiz, A. Clegg, J. Dong, E. Sucar, D. Novotny, M. Zollhoefer, and M. Mukadam, "iSDF: Real-Time Neural Signed Distance Fields for Robot Perception," *Robotics: Science and Systems*, 2022.
- [24] V. Vasilopoulos, S. Garg, J. Huh, B. Lee, and V. Isler, "HIO-SDF: Hierarchical incremental online signed distance fields," in *IEEE International Conference on Robotics and Automation*, 2024, pp. 17 537–17 543.
- [25] B. Bolte, A. Wang, J. Yang, M. Mukadam, M. Kalakrishnan, and C. Paxton, "USA-Net: Unified Semantic and Affordance Representations for Robot Memory," in *IEEE/RSJ International Conference on Intelligent Robots and Systems*, 2023, pp. 7141–7148.
- [26] P. Liu, K. Zhang, D. Tateo, S. Jauhari, J. Peters, and G. Chaitzaki, "Regularized Deep Signed Distance Fields for Reactive Motion Generation," in *IEEE/RSJ International Conference on Intelligent Robots and Systems*, 2022, pp. 6673–6680.
- [27] M. Koptev, N. Figueroa, and A. Billard, "Neural Joint Space Implicit Signed Distance Functions for Reactive Robot Manipulator Control," *IEEE Robotics and Automation Letters*, vol. 8, no. 2, pp. 480–487, 2023.
- [28] Y. Li, Y. Zhang, A. Razmjoo, and S. Calinon, "Representing robot geometry as distance fields: Applications to whole-body manipulation," in *IEEE International Conference on Robotics and Automation*, 2024, pp. 15 351–15 357.
- [29] J. Haviland and P. Corke, "Manipulator Differential Kinematics: Part I: Kinematics, Velocity, and Applications," *IEEE Robotics & Automation Magazine*, pp. 2–11, 2024.
- [30] T. Yoshikawa, "Manipulability of Robotic Mechanisms," *The International Journal of Robotics Research*, vol. 4, no. 2, pp. 3–9, 1985.
- [31] R. A. Newcombe, A. Fitzgibbon, S. Izadi, O. Hilliges, D. Molyneux, D. Kim, A. J. Davison, P. Kohi, J. Shotton, and S. Hodges, "KinectFusion: Real-time dense surface mapping and tracking," in *IEEE International Symposium on Mixed and Augmented Reality*, no. 4, 2011, pp. 127–136.
- [32] T. Takikawa, A. Glassner, and M. McGuire, "A Dataset and Explorer for 3D Signed Distance Functions," *Journal of Computer Graphics Techniques*, vol. 11, no. 2, 2022.
- [33] N. Sharp and A. Jacobson, "Spelunking the Deep: Guaranteed Queries on General Neural Implicit Surfaces via Range Analysis," *ACM Transactions on Graphics*, vol. 41, no. 4, 2022.
- [34] B. Faverjon and P. Tournassoud, "A local based approach for path planning of manipulators with a high number of degrees of freedom," in *IEEE International Conference on Robotics and Automation*, 1987, pp. 1152–1159.
- [35] P. Corke and J. Haviland, "Not your grandmother's toolbox - the Robotics Toolbox reinvented for Python," *IEEE International Conference on Robotics and Automation*, pp. 11 357–11 363, 2021.
- [36] B. Cohen, I. A. Sucan, and S. Chitta, "A generic infrastructure for benchmarking motion planners," in *IEEE/RSJ International Conference on Intelligent Robots and Systems*, 2012, pp. 589–595.
- [37] S. Gulati and B. Kuipers, "High performance control for graceful motion of an intelligent wheelchair," in *IEEE International Conference on Robotics and Automation*, 2008, pp. 3932–3938.
- [38] Y. Xie, T. Takikawa, S. Saito, O. Litany, S. Yan, N. Khan, F. Tombari, J. Tompkin, V. Sitzmann, and S. Sridhar, "Neural Fields in Visual Computing and Beyond," *Computer Graphics Forum*, vol. 41, no. 2, pp. 641–676, 2022.